ACS APPLIED MATERIALS & INTERFACES

Research Article

www.acsami.org

Microsized BiOCl Square Nanosheets as Ultraviolet Photodetectors and Photocatalysts

Min Li,[†,‡] Junying Zhang,[*,†] Hong Gao,[†] Feng Li,[‡] Sten-Eric Lindquist,[§] Nianqiang Wu,[∥] and Rongming Wang[⊥]

[†]Key Laboratory of Micro-nano Measurement, Manipulation and Physics (Ministry of Education), Department of Physics, Beihang University, Beijing 100191, China

[‡]School of Physics and Electronic Engineering, Taishan University, Taian, Shandong 271021, China

[§]Department of Physical Chemistry, Uppsala University, Uppsala S-75121, Sweden

[∥]Department of Mechanical and Aerospace Engineering, West Virginia University, Morgantown, West Virginia 26506-6106, United States

[⊥]School of Mathematics and Physics, University of Science and Technology Beijing, Beijing 100083, China

Supporting Information

ABSTRACT: BiOCl microstructures that include microspheres stacked by nanosheet and microsized square nanosheets, with a large lateral size of 3−5 μm and a thickness of 35 nm (the side length/thickness ratio is ∼100), are synthesized by a solvothermal method with the assistance of polyvinylpyrrolidone. The exposed face of the large square nanosheet is {001} facet. The BiOCl microstructures show good photocatalytic activity toward decomposition of Rhodamine B under ultraviolet−visible light irradiation. Moreover, individual microsized BiOCl square nanosheets are employed as the building block for construction of an ultraviolet photodetector. Because of its large size, thin thickness, and high surface-to-volume ratio, a BiOCl nanosheet shows high sensitivity and fast transient response to ultraviolet light in the spectral range 200−380 nm.

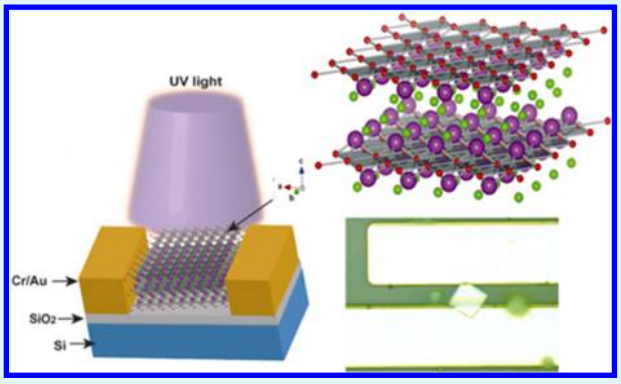

KEYWORDS: *BiOCl, ultraviolet photodetector, photocatalysis, optoelectronics, solvothermal*

1. INTRODUCTION

Photon detection in the ultraviolet (UV) region shows wide applications, including environmental and biological research, sensors, missile launching, and light detection. UV radiation emitted by the sun falls into the range 200−400 nm, which can be subdivided into three bands: UV−A (320−400 nm), UV−B (290−320 nm), and UV−C (200−290 nm). Development of a UV−A light detector and sensor is of particular importance because of the urgent demand in the iatric and microelectronic fields.[1,2] The bandgap of bismuth oxychloride (BiOCl) ranges from 3.0 to 3.5 eV, depending on the preparation method. In addition, the easily formed oxygen vacancies cause weak light response alongside the band-to-band absorption.[3−7] BiOCl could be a promising candidate material for UV−A light detection. With suitable cutoff filters, BiOCl can be used as a UV−A and UV−A plus UV−B detector. This study shows that the microsized (2−5 μm) BiOCl square nanosheets with a high side length/thickness ratio of ∼100 have advantages as a photodetector because they exhibit higher photosensitivity and faster transient response compared to their bulk counterparts, and it is convenient to build a microsized photodetector with a simple photolithography method.

Various BiOCl morphologies, including nanoflakes,[8] nanobelts,[9] nanosheets,[3] nanonetworks,[10] nanoflowers,[11] nanowires,[12] and microsphere hierarchical structures,[13−17] have been reported so far. Among these available BiOCl nanomaterials, two-dimensional (2D) nanosheet single crystals should be the most ideal building blocks for individual nanostructure-based devices due to their single-crystalline nature, well-defined shape, and highly exposed {001} facets. However, the lateral size of the reported BiOCl nanosheets has not been large enough so far,[3,18−20] and hence it has been difficult to deposit metal electrodes on the two ends of small-sized BiOCl nanostructure, even by the standard electron beam lithography (EBL) method. Compared with other dimensional micro-/nanostructures, 2D single-crystalline nanostructures have advantages in applications such as nanoelectronics and optoelectronics,[21,22] which favors the charge migration and suppresses the charge recombination. In particular, BiOCl consists of [Cl−Bi−O−Bi−Cl] layers stacked together by the

Received: January 3, 2016
Accepted: February 25, 2016
Published: February 25, 2016

DOI: 10.1021/acsami.6b00042
ACS Appl. Mater. Interfaces 2016, 8, 6662−6668

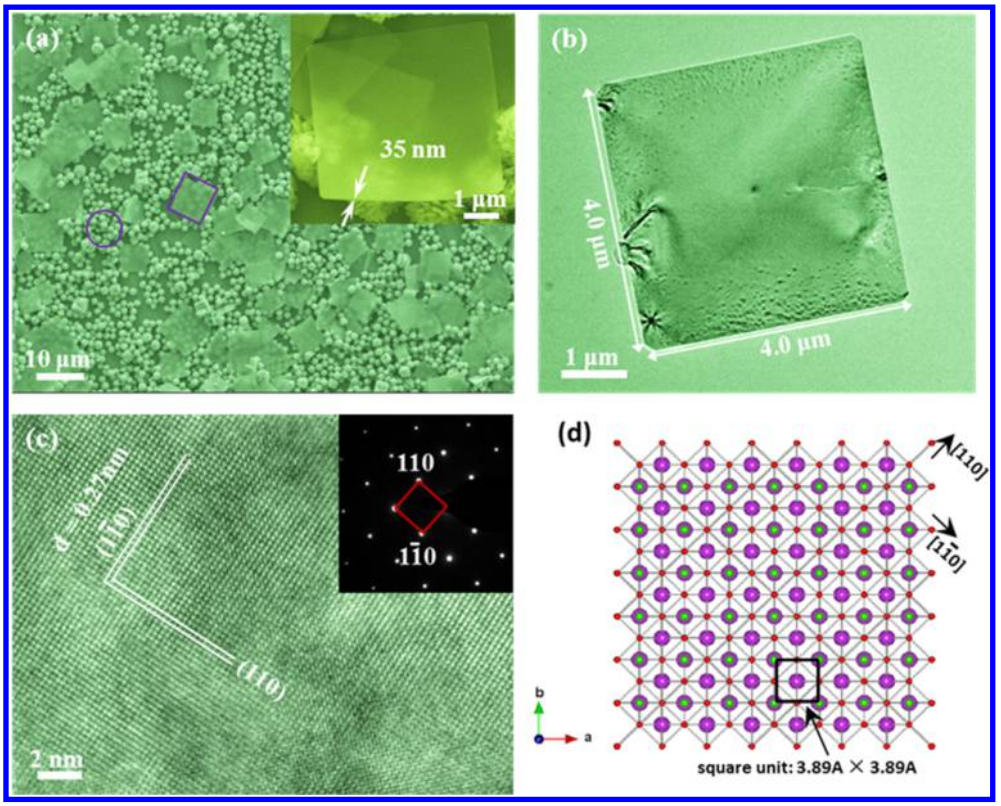

Figure 1. (a) FESEM image of BiOCl nanosheets. For further explanation see the text. (b) TEM and (c) HRTEM image of a single BiOCl nanosheet. Inset in (c) is the SAED pattern taken from this single nanosheet. (d) Schematic illustration of the BiOCl (001) plane (Bi atom, lilac; O atom, red; Cl atom, green).

nonbonding interaction through the Cl atoms along the *c*-axis, where $[Bi_2O_2]^{2+}$ layers are sandwiched between two slabs of halogen ions. Such a layered structure enables the effective separation of the photoinduced electrons and holes and promotes photocatalytic reactions.[23,24] To the best of our knowledge, there are limited studies on the optoelectronic properties of BiOCl nanostructures. Inspired by the successful preparation of a large-sized BiOCl nanosheet in this work, a low-cost photolithography route is employed to construct a UV-sensible photodetector.[2,25]

2. EXPERIMENTAL SECTION

Sample preparation. All the chemical reagents in this work were analytical-grade purity without further purification. In a typical synthesis, 0−1.5 g of polyvinylpyrrolidone (PVP) was dissolved in 40 mL of ethylene glycol (EG). Then, 0.97 g of $Bi(NO_3)_3{\cdot}5H_2O$ was added to the solution. Next, 0.268 g of NH_4Cl was added into the mixture, and the mixture was vigorously stirred for 30 min to ensure that all reagents were dispersed homogeneously. Subsequently, the solution was transferred into a Teflon-lined stainless steel autoclave with a capacity of 50 mL, sealed and heated at 170 °C in an electrical oven for 20 h, and then cooled naturally to room temperature. The precipitate was collected and washed with deionized water and ethanol repeatedly to remove the residual trace of reactants. Finally, the product was dried in an oven at 60 °C. The BiOCl microspheres assembled by irregular nanoplates were obtained without adding PVP (defined as "BiOCl−PVP-0"), while the hierarchical BiOCl microspheres assembled by single-crystalline square nanosheets were obtained by adding 1.5 g of PVP into the precursor (defined as "BiOCl−PVP-1.5"). The BiOCl microspheres plus microsized square nanosheets were obtained in the presence of 0.8 g of PVP in the precursor (defined as "BiOCl−PVP-0.8"). To understand the role of PVP and EG solvent during synthesis, several groups of control experiments were also carried out with the same procedures, by changing the amount of PVP and replacing the EG by distilled water, from which the product obtained was defined as "BiOCl−H_2O".

Characterization. An X-ray diffractometer (XRD, Panalytical X'pert pro mpd) with a Cu Kα source was used to determine the crystal structure of the samples. The microstructure of the product was characterized by field-emission scanning electron microscopy (FESEM, Hitachi S-4800 and ZEISS, MERLIN VP Compact). Transmission electron microscopy (TEM) images and high-resolution TEM images were obtained using Tecnai G2 F30 S-TWIN with an accelerating voltage of 200 kV. The specific area of the samples was obtained by recording the adsorption−desorption isotherms at the liquid-nitrogen temperature of 77 K using a nitrogen-adsorption system (Quantachrome, NOVA 2200e). Ultraviolet−visible (UV−vis) diffuse reflectance spectrum was measured with HITACHI U-3010. $BaSO_4$ was used as a reflectance standard sample.

Photocatalysis testing. The photocatalytic activity of the samples was examined by measuring the decomposition rate of Rhodamine B (RhB) in aqueous solution. Typically, 20 mg of photocatalysts were added into 100 mL of 10 mg/L RhB aqueous solution. Before illumination, the suspension was placed in the dark under constant stirring for 60 min to reach adsorption/desorption equilibrium. Then, the RhB solution was irradiated with a 300 W Xe lamp with the average light intensity of 100 mW/cm^2 striking on the surface of the reaction solution. Next, 4 mL of the suspension was withdrawn every 20 min under irradiation and centrifuged to remove the photocatalyst for UV−vis absorption measurements. The concentration of RhB was determined by monitoring its characteristic light absorption at 552 nm.

Photodetection. A pair of Au/Cr electrodes were deposited on an oxidized Si wafer substrate with a 200-nm-thick SiO_2 layer through a photolithography, electron-beam deposition and lift-off process.[2] Sample BiOCl−PVP-0.8 was dispersed in ethanol and then dropped on the Au/Cr electrode surface, followed by air-drying at 60 °C. The nanosheet with large size (>3 μm) could be easily identified and moved to bridge the holder of the microphotodetector. The current−voltage (I−V) characteristics of the BiOCl nanosheet-based photo-

DOI: 10.1021/acsami.6b00042
ACS Appl. Mater. Interfaces 2016, 8, 6662−6668

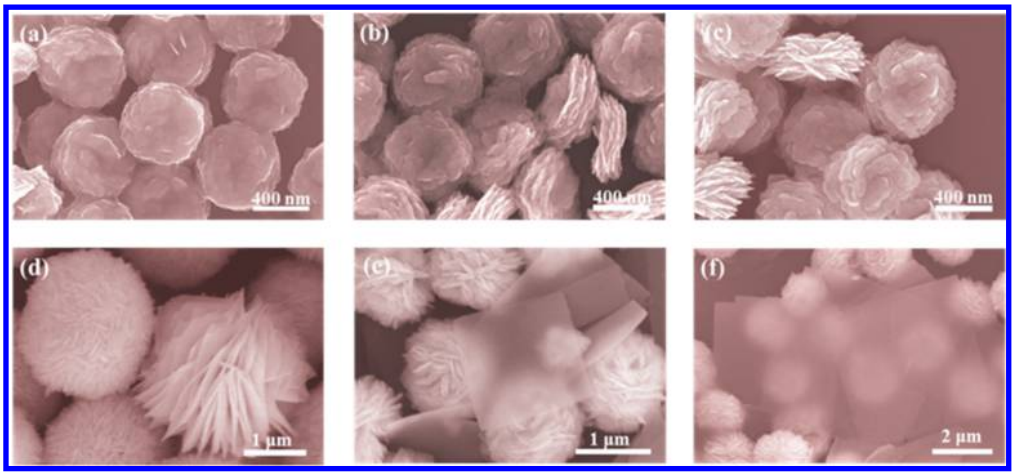

Figure 2. Morphology of the BiOCl–PVP-0.8 sample after different intervals of solvothermal treatment: (a) 2 h, (b) 4 h, (c) 8 h, (d, e) 12 h, and (f) 24 h.

detector were measured using a photoelectrochemical workstation (Germany ZAHNER) and semiconductor characterization system (Keithley 4200-SCS). The light response of the device was recorded under illumination using a xenon lamp (500 W).

3. RESULTS AND DISCUSSION

The morphologies of the as-prepared products were first investigated by field-emission scanning electron microscopy (FESEM). The panoramic views of the sample noted as BiOCl–PVP-0.8 revealed that a large number of nanosheets were formed (Figure 1a, marked by a lilac square). A zoom-in image (the inset in Figure 1a) further confirms that the nanosheets were well-grown with regular square shapes, sharp corners, and smooth surfaces. The thickness of the square-shaped nanosheets was estimated to ~35 nm as seen from SEM in the inset in Figure 1a and the images in Figure S1 in Supporting Information, while the mean length of their sides was as large as 4.0 μm (giving a side length/thickness ratio of ~100). These nanosheets were much larger and more regular than the samples with similar thickness reported in the previous studies,[3,18] which is good for construction of functional nanodevices from individual nanosheets. Some hierarchical flower-like microspheres, which were assembled tightly by thin sheets with the size of several hundred nanometers (the lilac circle in Figure 1a), coexisted in the collected product. The major part of the microspheres was still intact even after a lengthy (tens of minutes) ultrasonic treatment, indicating the stable self-assembly nature. Figure 1b reveals the transmission electron microscopy (TEM) image of a single square nanosheet, indicating its square shape. High-resolution transmission electron microscopy (HRTEM) and the corresponding selected-area electron diffraction (SAED) pattern characterization were performed on the edge of the sheet (Figure 1c). The continuous lattice fringes show two sets of perpendicular lattice spacing of ~0.27 nm that correspond to the (110) and $(1\bar{1}0)$ planes of tetragonal BiOCl, respectively. The clear two-dimensional lattice fringe demonstrates the high crystallinity and smooth exposed facet of such a large nanosheet. The sharp diffraction spots in the SAED can be well-indexed to the reflection of the tetragonal BiOCl < 001> axis. Because the nanosheets generally lay flat on the copper grid, perpendicular to the electron beam, the observed diffraction spots of the <001> zone axis indicate that the exposed top surface of each nanosheet is (001) plane. A schematic diagram is presented in Figure 1d to describe the (001) plane structure with high-density oxygen atoms. One can see that the minimum unit in the (001) plane was in the shape of a square, as labeled by solid black lines. Such a square lattice unit consists of four Bi–Bi bonds with a size of 3.89 Å × 3.89 Å. The top and exposed face of (001) plane for the microsized BiOCl square nanosheet indicates the in-plane growth mechanism reported by other groups.[26,27]

To understand the growth process, time-dependent experiments were carried out and the resulting products collected at different stages were analyzed by FESEM. After 2 h of solvothermal treatment, the BiOCl particles nucleated and grew to the nanosized erythrocyte-like particles (Figure 2a). With prolonged time (4 h), the erythrocyte-shape particles were evolved into the nanoflake-assembled flowers as indicated in Figure 2b. Obviously, these hierarchical structures were gradually formed and became more pronounced with prolonged time (Figure 2c) due to the well-known Oswald ripening process.[28] After 12 h, a mixture of three different microstructures appeared, including (i) the microsphere tightly composed of nanosheets, (ii) the large-sized square nanosheets, and (iii) the 3D hierarchical structures assembled loosely by nanosheets (Figure 2d and e). Because the crystal growth depends strongly on the concentration of the species in the liquid surrounding the crystal,[29] the growth of nanoflakes in this process can be attributed to the concentration change in the supersaturated solution. The BiOCl micro-/nanocrystals tend to form lamellar shapes as the initial unit of structure.[3,30] With prolongation of the solvothermal time to 24 h, the hierarchical BiOCl structure that was loosely assembled by nanosheets disappears (Figure 2f). The BiOCl microspheres coexisted with larger single-crystalline quadrilateral nanosheets. Hence, it can be concluded that prolonging the solvothermal time leads to evolution of the single-crystalline square nanosheets into the loose hierarchical structure. The evolution from microsphere to large nanosheets may have a relation to the crystal structure of BiOCl. As mentioned above, BiOCl consisted of [Cl–Bi–O–Bi–Cl] layers loosely stacked together by the nonbonding interaction through the Cl atoms along the *c*-axis, where $[Bi_2O_2]^{2+}$ layers were sandwiched between two slabs of halogen ions. The NH_4^+ and H^+ ions in the solution may adsorb on the facets covered by Cl^-. Electrostatic repulsion can then lead to the separation of nanosheets from the loose hierarchical structure. For the BiOCl microstructure,

DOI: 10.1021/acsami.6b00042
ACS Appl. Mater. Interfaces 2016, 8, 6662–6668

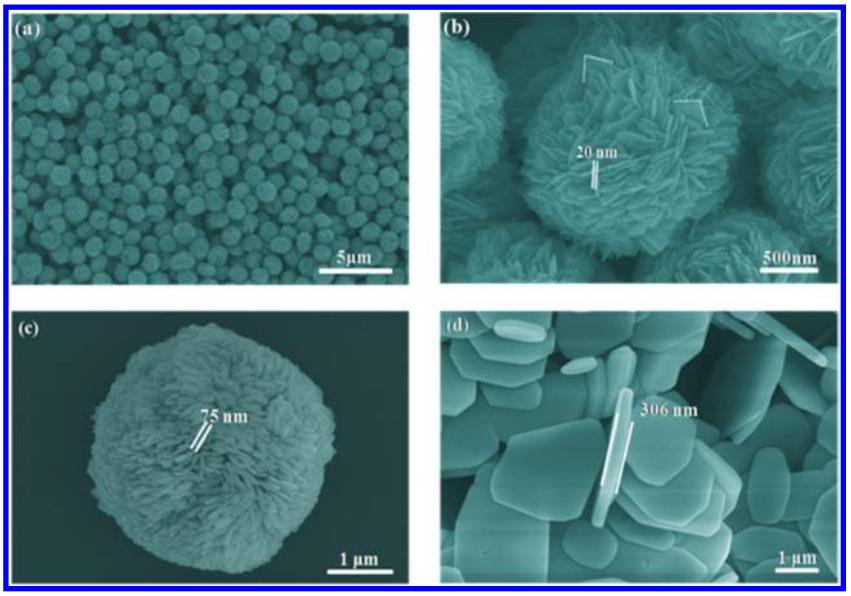

Figure 3. FE-SEM images of the BiOCl products: (a, b) BiOCl–PVP-1.5, (c) BiOCl–PVP-0, and (d) BiOCl–H_2O.

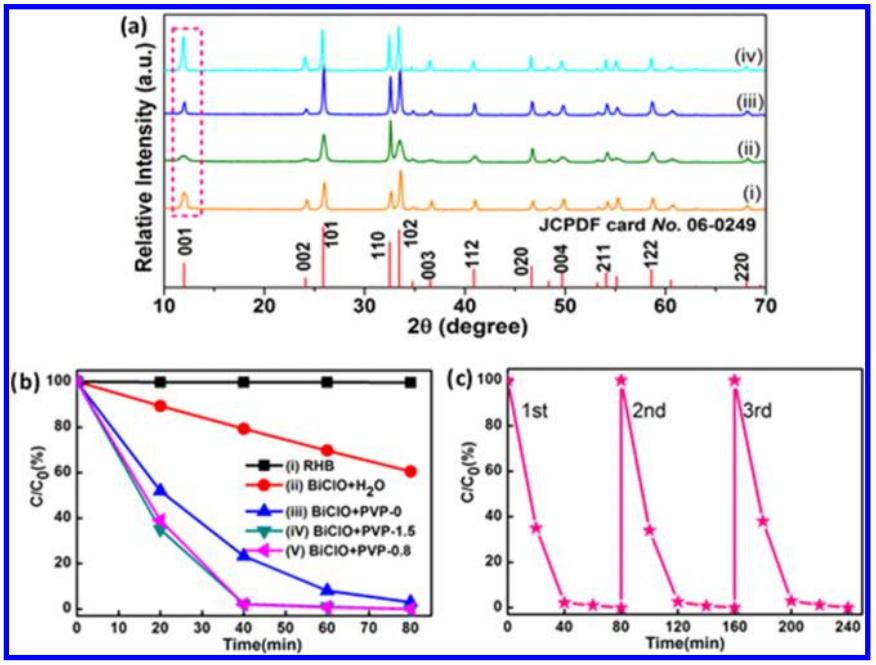

Figure 4. (a) XRD patterns of the as-synthesized BiOCl samples: (i) BiOCl–H_2O, (ii) BiOCl–PVP-0, (iii) BiOCl–PVP-1.5, and (iv) BiOCl–PVP-0.8. (b) Comparison of the degradation rate of RhB with different BiOCl structures under UV–visible light irradiation. (c) Cycling curves of photocatalytic degradation of RhB with BiOCl–PVP-0.8 as the photocatalyst.

the acidity in the solution is also a key factor influencing crystal growth, which can affect the aggregation of the nanosheets.[31]

It is well-known that PVP is a common surfactant that can function not only as potential face inhibitors but also as a stabilizer by coordinating with both nitrogen and oxygen atoms in the polar pyrrolidone groups.[32−34] Different amounts of PVP ranging from 0 to 1.5 g were added while keeping other conditions constant. With adding 1.5 g of PVP (BiOCl–PVP-1.5), the large-sized BiOCl nanosheets disappeared, leaving only the uniform microspheres (~1.5 μm in diameter) stacked by a small-sized square nanosheet with a thickness of 20 nm (Figure 3a and b). Without adding any PVP (BiOCl–PVP-0), uniform microspheres with a larger size (diameter ≈ 3.0 μm) were observed in Figure 3c. Careful observation reveals that such architecture consists of irregular nanopanels with a thickness of ~75 nm. Different amounts of PVP (such as 0.1, 0.5, 1.0, and 1.3 g) were used to obtain a PVP concentration threshold at which only large-sized BiOCl square nanosheets were formed favorably (Figure S2 in Supporting Information). Unfortunately, the percentage of large-sized BiOCl square nanosheets reached the highest value (roughly 40–50% in quality) when using 0.8 g of PVP. When the solvent of EG was replaced by distilled water in the absence of any PVP, only the irregular nano-/micropanels with a size of 0.5–3.0 μm and a thickness of 0.3 μm were obtained (BiOCl–H_2O), as demonstrated in Figure 3d.

Figure 4a shows the X-ray diffraction (XRD) patterns of the as-prepared BiOCl samples. The sharp peaks in the XRD

DOI: 10.1021/acsami.6b00042
ACS Appl. Mater. Interfaces 2016, 8, 6662–6668

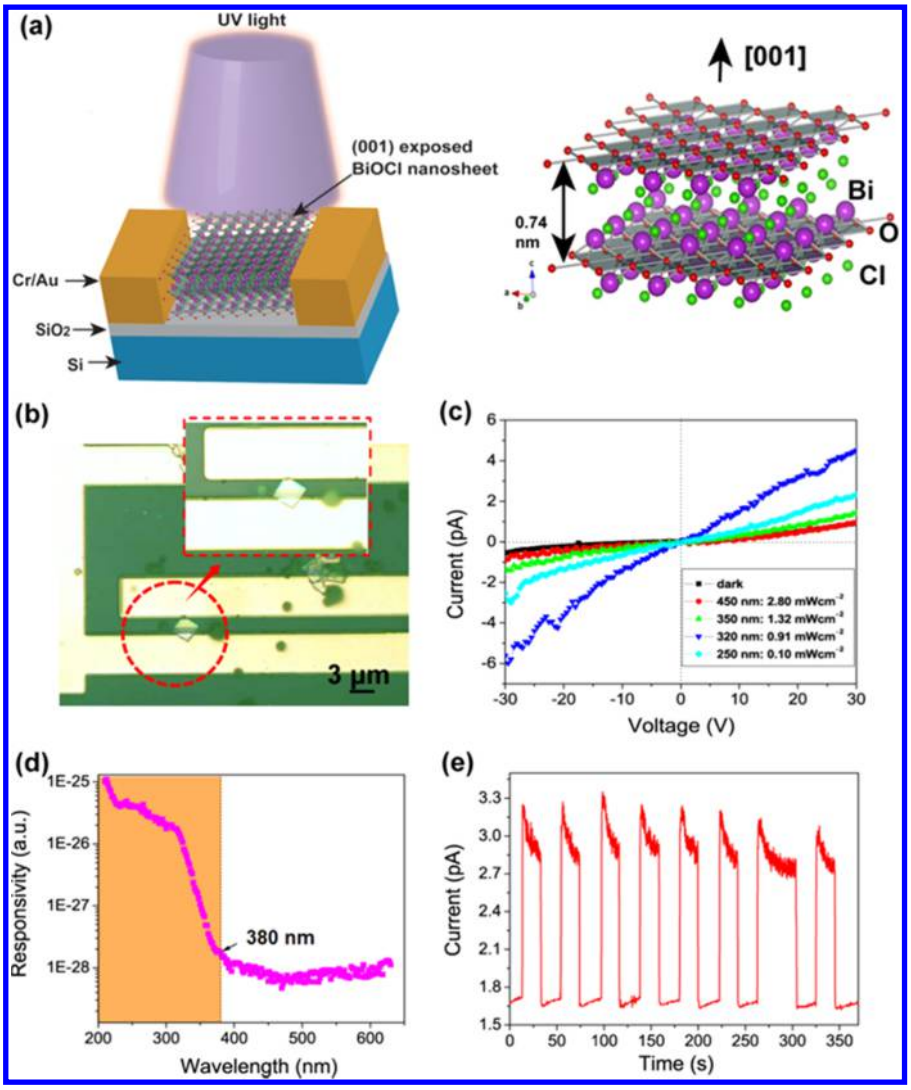

Figure 5. (a) (Left) Schematic illustration of an individual BiOCl-nanosheet device. (Right) 3-Dimensional model of the suggested crystal structure of the BiOCl-nanosheet. (b) Corresponding optical microscopy image of the device with a high-resolution image inserted. (c) Typical $I-V$ curves of the device in the dark and under light illumination with varied wavelengths of 450, 350, 320, and 250 nm. (d) Spectral distribution of the photoresponse in terms of responsivity of the same device at a bias of 30.0 V. (e) On/off switching of the device upon pulsed illumination under 320 nm light with a power density of 0.91 mW/cm^2.

patterns indicate good crystallity of the BiOCl–H_2O, BiOCl–PVP-0, BiOCl–PVP-1.5, and BiOCl–PVP-0.8 samples. All the diffraction peaks can be indexed to the tetragonal BiOCl with a space group $P4/nmm$ (a = 0.3891 nm, c = 0.7369 nm; JCPDS card no. 06-02490, the orange line). It can be clearly observed that the diffraction peak intensity of the (001) plane of the BiOCl–PVP-0.8 sample was relatively stronger than that of the other samples (BiOCl–PVP-0 and BiOCl–PVP-1.5), which can be properly explained on the basis of the crystallographic nature and morphology of the BiOCl crystals. The relatively thinner thickness and the large size for microsized BiOCl nanosheets reflect the more exposed areas of {001} facets, which is in good accordance with the SEM and TEM observation results.

The UV–visible diffuse reflectance spectra (Figure S3) show that the light absorption edge had a slight red-shift for the BiOCl–PVP-0 sample, which should be attributed to the increased thickness of the nanosheet. The photocatalytic activity of BiOCl samples was evaluated by degradation of Rhodamine B (RhB) in a 10 mg/L aqueous solution under UV–visible light irradiation (Figure 4b). After light irradiation for 40 min, photodegradation of RhB reached 97% for BiOCl–PVP-1.5 and BiOCl–PVP-0.8 samples, which compared favorably to the value of 75% for the BiOCl–PVP-0 sample. The BiOCl–H_2O sample, consisting of irregular and nonuniform BiOCl plates, exhibited very low photocatalytic activity compared to other samples. Apparently, the BiOCl–PVP-1.5 and BiOCl–PVP-0.8 samples showed nearly the same trend, which indicated the highest photocatalytic activity. The BiOCl–PVP-0 sample took second place, followed by the BiOCl–H_2O. These results were consistent with the Brunauer–Emmett–Teller (BET) results as shown in Table S1 in Supporting Information (23.8 m^2/g for BiOCl–PVP-0.8, 20.84 m^2/g for BiOCl–PVP-1.5, and 8.03 m^2/g for BiOCl–PVP-0). It can be concluded that the sample with the larger special surface area (SSA) possesses the higher photocatalytic activity. The photocatalytic process is related to the adsorption and desorption of molecules on the surface of the catalyst.[35,36] The adsorption behaviors of these samples for RhB were also studied before irradiation in the dark (Figure S4 in Supporting

DOI: 10.1021/acsami.6b00042
ACS Appl. Mater. Interfaces 2016, 8, 6662–6668

Information). The results indicate that the adsorption process made partial contribution, although the proportion was <20%. Therefore, the higher specific surface area helps an increase in the rate of the photocatalytic reaction and promotes an efficient electron−hole separation.[37] In addition to the different SSAs, the surface structure of the nanostructure, such as the percentage of highly reactive {001} facets in the sample, also had a substantial positive effect on the photocatalytic activity.

The features such as large size, thin thickness, and high exposed active facet for this BiOCl nanosheet derived from the BiOCl−PVP-0.8 sample inspired us to build a microphotodetector. Thus, the microsized BiOCl nanosheets were employed as the building blocks for construction of a photodetector device as shown in Figure 5a and b. The $I-V$ curves of the device were measured by a two-probe method under ambient air conditions both in the dark and under illumination of light with different wavelengths (Figure 5c). The dark current of the device was as low as 0.94 pA at an applied voltage of 30.0 V. No obvious photocurrent was detected under illumination of light longer than 450 nm. In contrast, the photocurrent increased when the wavelength of incident light fell into the UV−A region. The indirect optical bandgap (E_g) of the present BiOCl nanosheets sample was determined to be 3.50 eV (corresponding to 354 nm) using a Tauc plot (Figure S5 in Supporting Information). Although the concept of demarcation energy (E_d) is only useful for the qualitative, rather than the quantitative, analysis, it is interesting to note that E_d (derived from a ln α vs $h\nu$ plot) = 3.55 eV was almost the same value as E_g. Accordingly, the photocurrent induced by the light at a wavelength of 350 nm was ascribed to the electron−hole pairs generated by the incident photons with energy larger than the bandgap. Because BiOCl has an indirect-transition bandgap, the phonon-assisted near-edge absorption extended the photoresponse to a longer wavelength. The anodic photocurrent reached a maximum value of 4.68 pA at 320 nm, while the cathodic photocurrent was 6 pA at the same wavelength. At a shorter wavelength (250 nm), the photocurrent was reduced, which can be attributed to the smaller power density (0.10 mW/cm^2) of light source at this wavelength. The linear shape of the $I-V$ provides evidence in accordance to theory (the gain = $G = \tau\mu V/L^2$) that G is proportional to V.[38] (In the equation τ is the lifetime of the free carrier, μ is the mobility, and L is the electrode spacing.) Figure 5d displays the spectral photoresponse of the device at a bias of 30.0 V at different wavelengths from 200 to 630 nm. The sensitivity was very low when the wavelength was >400 nm. At shorter wavelengths, below 380 nm down to 200 nm, the responsivity gradually increased by ∼3 orders of magnitude. Besides light absorption ascribed to the interband electronic transition, the oxygen vacancies with states in the bandgap were prone to form.[6,7] These defect states can cause sub-bandgap transitions, which is responsible for the visible light absorption (Figure S3). As a result, weak photocurrent appeared under 450 nm irradiation (Figure 5c) and low photoresponsivity was observed in the range from 450 to 380 nm (Figure 5d). Figure 5e presents the transient photoresponse of the photodetector measured under light irradiation at 320 nm. Upon illumination, the photocurrent rapidly increased to 3.3 pA. It then rapidly decreased to its initial level when the light was turned off, showing the reproducible characteristics and fast response of the device. The experimental result shows that the transient time response of the present device was faster than the limit of the response of the used setup (0.3 s). The photocurrent was decayed from ∼3.3 to ∼2.8 pA after turning on the light. This decay was due to the filling of carrier traps in the bandgap in the samples. Furthermore, the current of this device was slowly recovered to a steady-state current in the dark by an opposite transient mainly due to charge recombination. However, we cannot exclude the possibility that the current transient was affected to some extent by the surface absorption/desorption phenomena and the charge redistribution.[39]

4. CONCLUSIONS

In summary, BiOCl microstructures that include microspheres stacked by nanosheet and microsized square nanosheets with a large lateral size of 3−5 μm and a thickness of 35 nm (the side/thickness ratio is ∼100) were successfully prepared. The BiOCl microspheres stacked by a smaller-sized nanosheet coexisted and were hard to eliminate despite extensive efforts, including varying the amount of PVP. However, the coexistence of the microspheres did not jeopardize the construction of the microphotodetector. Individual BiOCl-nanosheets derived from the BiOCl microstructures could be mounted in the gap between two metal (Au/Cr) electrodes. This BiOCl-nanosheet-based device was sensitive to ultraviolet light in the spectral range of 200−380 nm. In addition, photocatalytic testing results showed that the BiOCl microstructures were able to photodegrade RhB under UV−visible light irradiation more effectively than other samples, such as BiOCl microspheres and irregular nanopanels.

■ ASSOCIATED CONTENT

Supporting Information

The Supporting Information is available free of charge on the ACS Publications website at DOI: 10.1021/acsami.6b00042.

SEM images and UV−visible absorption spectra (PDF)

■ AUTHOR INFORMATION

Corresponding Author

*E-mail: zjy@buaa.edu.cn.

Notes

The authors declare no competing financial interest.

■ ACKNOWLEDGMENTS

This work was supported by the Ph.D. Programs Foundation of the Ministry of Education of China (Grant no. 20121102110027), the National Natural Science Foundation of China (Grant nos. 91222110, 51472013, 11174215, and 11547140), the Shandong Provincial Natural Science Foundation (no. ZR2015EL007), and the Beijing Key Discipline Foundation of Condensed Matter Physics.

■ REFERENCES

(1) Fang, X. S.; Bando, Y.; Liao, M. Y.; Gautam, U. K.; Zhi, C. Y.; Dierre, B.; Liu, B. D.; Zhai, T. Y.; Sekiguchi, T.; Koide, Y.; Golberg, D. Single-Crystalline ZnS Nanobelts as Ultraviolet-Light Sensors. *Adv. Mater.* **2009**, *21*, 2034−2039.

(2) Fang, X. S.; Hu, L. F.; Huo, K. F.; Gao, B.; Zhao, L. J.; Liao, M. Y.; Chu, P. K.; Bando, Y.; Golberg, D. New Ultraviolet Photodetector Based on Individual Nb_2O_5 Nanobelts. *Adv. Funct. Mater.* **2011**, *21*, 3907−3915.

(3) Jiang, J.; Zhao, K.; Xiao, X. Y.; Zhang, L. Z. Synthesis and Facet-Dependent Photoreactivity of BiOCl Single-Crystalline Nanosheets. *J. Am. Chem. Soc.* **2012**, *134*, 4473−4476.

(4) Cheng, H. F.; Huang, B. B.; Qin, X. Y.; Zhang, X. Y.; Dai, Y. A Controlled Anion Exchange Strategy to Synthesize Bi_2S_3 Nanocryst-

DOI: 10.1021/acsami.6b00042
ACS Appl. Mater. Interfaces 2016, 8, 6662−6668

als/BiOCl Hybrid Architectures with Efficient Visible Light Photoactivity. *Chem. Commun.* **2012**, *48*, 97−99.
(5) Wang, D. H.; Gao, G. Q.; Zhang, Y. W.; Zhou, L. S.; Xu, A. W.; Chen, W. Nanosheet-Constructed Porous BiOCl with Dominant {001} Facets for Superior Photosensitized Degradation. *Nanoscale* **2012**, *4*, 7780−7785.
(6) Ye, L. Q.; Zan, L.; Tian, L. H.; Peng, T. Y.; Zhang, J. J. The {001} Facets-Dependent High Photoactivity of BiOCl Nanosheets. *Chem. Commun.* **2011**, *47*, 6951−6953.
(7) Zhao, K.; Zhang, L. Z.; Wang, J. J.; Li, Q. X.; He, W. W.; Yin, J. J. Surface Structure-Dependent Molecular Oxygen Activation of BiOCl Single-Crystalline Nanosheets. *J. Am. Chem. Soc.* **2013**, *135*, 15750−15753.
(8) Armelao, L.; Bottaro, G.; Maccato, C.; Tondello, E. Bismuth Oxychloride Nanoflakes: Interplay between Composition-Structure and Optical Properties. *Dalton Trans.* **2012**, *41*, 5480−5485.
(9) Peng, H. L.; Chan, C. K.; Meister, S.; Zhang, X. F.; Cui, Y. Shape Evolution of Layer-Structured Bismuth Oxychloride Nanostructures via Low-Temperature Chemical Vapor Transport. *Chem. Mater.* **2009**, *21*, 247−252.
(10) Guo, C. F.; Zhang, J. M.; Tian, Y.; Liu, Q. A General Strategy to Superstructured Networks and Nested Self-Similar Networks of Bismuth Compounds. *ACS Nano* **2012**, *6*, 8746−8752.
(11) Song, J. M.; Mao, C. J.; Niu, H. L.; Shen, Y. H.; Zhang, S. Y. Hierarchical Structured Bismuth Oxychlorides: Self-Assembly from Nanoplates to Nanoflowers via a Solvothermal Route and their Photocatalytic Properties. *CrystEngComm* **2010**, *12*, 3875−3881.
(12) Wu, S. J.; Wang, C.; Cui, Y. F.; Wang, T. M.; Huang, B. B.; Zhang, X. Y.; Qin, X. Y.; Brault, P. Synthesis and Photocatalytic Properties of BiOCl Nanowire Arrays. *Mater. Lett.* **2010**, *64*, 115−118.
(13) Lei, Y. Q.; Wang, G. H.; Song, S. Y.; Fan, W. Q.; Zhang, H. J. Synthesis, Characterization and Assembly of BiOCl Nanostructure and Their Photocatalytic Properties. *CrystEngComm* **2009**, *11*, 1857−1862.
(14) Li, J. F.; Zhu, Y. C.; Yan, Y.; Xi, B. J.; Tang, K. B.; Qian, Y. T. Solvothermal Synthesis of 3D BiOCl Microstructures and their Electrochemical Hydrogen Storage Behavior. *J. Nanosci. Nanotechnol.* **2012**, *12*, 2068−2075.
(15) Zhang, X.; Ai, Z. H.; Jia, F. L.; Zhang, L. Z. Generalized One-Pot Synthesis, Characterization, and Photocatalytic Activity of Hierarchical BiOX (X = Cl, Br, I) Nanoplate Microspheres. *J. Phys. Chem. C* **2008**, *112*, 747−753.
(16) Peng, S.; Li, L.; Zhu, P.; Wu, Y.; Srinivasan, M.; Mhaisalkar, S. G.; Ramakrishna, S.; Yan, Q. Controlled Synthesis of BiOCl Hierarchical Self-Assemblies with Highly Efficient Photocatalytic Properties. *Chem. - Asian J.* **2013**, *8*, 258−268.
(17) Xia, J. X.; Xu, L.; Zhang, J.; Yin, S.; Li, H. M.; Xu, H.; Di, J. Improved Visible Light Photocatalytic Properties of Fe/BiOCl Microspheres Synthesized via Self-doped Reactable Ionic Liquids. *CrystEngComm* **2013**, *15*, 10132−10141.
(18) Guan, M. L.; Xiao, C.; Zhang, J.; Fan, S. J.; An, R.; Cheng, Q. M.; Xie, J. F.; Zhou, M.; Ye, B. J.; Xie, Y. Vacancy Associates Promoting Solar-Driven Photocatalytic Activity of Ultrathin Bismuth Oxychloride Nanosheets. *J. Am. Chem. Soc.* **2013**, *135*, 10411−10417.
(19) Gao, M. C.; Zhang, D. F.; Pu, X. P.; Li, M. T.; Yu, Y. M.; Shim, J. J.; Cai, P. Q.; Kim, S.; Seo, H. J. Combustion Synthesis of BiOCl with Tunable Percentage of Exposed {001} Facets and Enhanced Photocatalytic Properties. *J. Am. Ceram. Soc.* **2015**, *98*, 1515−1519.
(20) Ye, L. Q.; Jin, X. L.; Leng, Y. M.; Su, Y. R.; Xie, H. Q.; Liu, C. Synthesis of Black Ultrathin BiOCl Nanosheets for Efficient Photocatalytic H_2 Production under Visible Light Irradiation. *J. Power Sources* **2015**, *293*, 409−415.
(21) Butler, S. Z.; Hollen, S. M.; Cao, L. Y.; Cui, Y.; Gupta, J. A.; Gutiérrez, H. R.; Heinz, T. F.; Hong, S. S.; Huang, J. X.; Ismach, A. F.; Johnston-Halperin, E.; Kuno, M.; Plashnitsa, V. V.; Robinson, R. D.; Ruoff, R. S.; Salahuddin, S.; Shan, J.; Shi, L.; Spencer, M. G.; Terrones, M.; Windl, W.; Goldberger, J. E. Progress, Challenges, and Opportunities in Two-Dimensional Materials Beyond Graphene. *ACS Nano* **2013**, *7*, 2898−2926.
(22) Wang, Q. H.; Kalantar-Zadeh, K.; Kis, A.; Coleman, J. N.; Strano, M. S. Electronics and Optoelectronics of Two-Dimensional Transition Metal Dichalcogenides. *Nat. Nanotechnol.* **2012**, *7*, 699−712.
(23) Lin, X. P.; Huang, T.; Huang, F. Q.; Wang, W. D.; Shi, J. L. Photocatalytic Activity of a Bi-Based Oxychloride Bi_3O_4Cl. *J. Phys. Chem. B* **2006**, *110*, 24629−24634.
(24) Cheng, H.; Huang, B.; Wang, Z.; Qin, X.; Zhang, X.; Dai, Y. One-Pot Miniemulsion-Mediated Route to BiOBr Hollow Microspheres with Highly Efficient Photocatalytic Activity. *Chem. - Eur. J.* **2011**, *17*, 8039−8043.
(25) Peng, L.; Hu, L. F.; Fang, X. S. Low-Dimensional Nanostructure Ultraviolet Photodetectors. *Adv. Mater.* **2013**, *25*, 5321−5328.
(26) Geng, F. X.; Xin, H.; Matsushita, Y.; Ma, R.; Tanaka, M.; Izumi, F.; Iyi, N.; Sasaki, T. New Layered Rare-Earth Hydroxides with Anion-Exchange Properties. *Chem. - Eur. J.* **2008**, *14*, 9255−9260.
(27) Hu, L. F.; Ma, R. Z.; Ozawa, T. C.; Sasaki, T. Synthesis of a Solid Solution Series of Layered $Eu_xGd_{1-x}(OH)_{2.5}Cl_{0.5}\cdot 0.9H_2O$ and its Transformation into $(Eu_xGd_{1-x})_2O_3$ with Enhanced Photoluminescence Properties. *Inorg. Chem.* **2010**, *49*, 2960−2968.
(28) Politi, Y.; Arad, T.; Klein, E.; Weiner, S.; Addadi, L. Sea Urchin Spine Calcite Forms via a Transient Amorphous Calcium Carbonate Phase. *Science* **2004**, *306*, 1161−1164.
(29) Burton, W. K.; Cabrera, N.; Frank, F. C. The Growth of Crystals and the Equilibrium Structure of their Surfaces. *Philos. Trans. R. Soc., A* **1951**, *243*, 299−358.
(30) McCarty, K. F.; Bartelt, N. C. Crystal Growth Rate Limited by Step Length—the Case of Oxygen-Deficient TiO_2 Exposed to Oxygen. *J. Cryst. Growth* **2004**, *270*, 691−698.
(31) Zhang, K.; Liang, J.; Wang, S.; Liu, J.; Ren, K. X.; Zheng, X.; Luo, H.; Peng, Y. Y.; Zou, X.; Bo, X.; Li, J. H.; Yu, X. B. BiOCl Sub-Microcrystals Induced by Citric Acid and their High Photocatalytic Activities. *Cryst. Growth Des.* **2012**, *12*, 793−803.
(32) Tian, L.; Yao Tan, H.; Vittal, J. J. Morphology-Controlled Synthesis of Bi_2S_3 Nanomaterials via Single- and Multiple-Source Approaches. *Cryst. Growth Des.* **2008**, *8*, 734−738.
(33) Xue, H.; Li, Z. H.; Dong, H.; Wu, L.; Wang, X. X.; Fu, X. Z. 3D Hierarchical Architectures of $Sr_2Sb_2O_7$: Hydrothermal Syntheses, Formation Mechanisms, and Application in Aqueous-Phase Photocatalysis. *Cryst. Growth Des.* **2008**, *8*, 4469−4475.
(34) Li, Y. Q.; Wang, Z. Y.; Huang, B. B.; Dai, Y.; Zhang, X. Y.; Qin, X. Y. Synthesis of BiOBr-PVP Hybrids with Enhanced Adsorption-Photocatalytic Properties. *Appl. Surf. Sci.* **2015**, *347*, 258−264.
(35) Tan, C. W.; Zhu, G. Q.; Hojamberdiev, M.; Okada, K.; Liang, J.; Luo, X. C.; Liu, P.; Liu, Y. Co_3O_4 Nanoparticles-Loaded BiOCl Nanoplates with the Dominant {001} Facets: Efficient Photodegradation of Organicdyes under Visible Light. *Appl. Catal., B* **2014**, *152*−*153*, 425−436.
(36) Jiang, J.; Zhao, K.; Xiao, X. Y.; Zhang, L. Z. Synthesis and Facet-Dependent Photoreactivity of BiOCl Single-Crystalline Nanosheets. *J. Am. Chem. Soc.* **2012**, *134*, 4473−4476.
(37) Zhang, L.; Wang, W.; Zhou, L.; Xu, H. Bi_2WO_6 Nano- and Microstructures: Shape Control and Associated Visible-Light-Driven Photocatalytic Activities. *Small* **2007**, *3*, 1618−1625.
(38) Sze, S. M. In *Semiconductor Device Physics and Technology*, 2nd ed.; John Wiley & Sons: 2002.
(39) Hu, L. F.; Yan, J.; Liao, M. Y.; Wu, L. M.; Fang, X. S. Ultrahigh External Quantum Efficiency from Thin SnO_2 Nanowire Ultraviolet Photodetectors. *Small* **2011**, *7*, 1012−1017.

DOI: 10.1021/acsami.6b00042
ACS Appl. Mater. Interfaces 2016, 8, 6662−6668